Sensors and Materials, Vol. 35, No. 9 (2023) 3173–3188
MYU Tokyo

S & M 3383

Implantable Multimodal Sensing Device for Simultaneous Imaging and Electrophysiological Recording of Mouse Brain Activity

Kenji Sugie,[1] Kiyotaka Sasagawa,[1*] Ryoma Okada,[1] Yasumi Ohta,[1] Hironari Takehara,[1] Makito Haruta,[1] Hiroyuki Tashiro,[1,2] and Jun Ohta[1]

[1]Division of Materials Science, Graduate School of Science and Technology, Nara Institute of Science and Technology, 8916-5 Takayama, Ikoma, Nara 630-0192, Japan
[2]Department of Health Science, Faculty of Medical Sciences, Kyushu University, 3-1-1, Maidashi, Higashi-ku, Fukuoka 812-8582, Japan

(Received November 24, 2022; accepted December 26, 2022)

Keywords: implantable device, multimodal sensor, neural recording, CMOS image sensor

Optical and electrophysiological measurements help us understand mouse brain functions. One type of device available for optical measurements is an implantable complementary metal-oxide-semiconductor (CMOS) image sensor (ICIS). However, an ICIS alone cannot directly measure the electrical signals emitted by mouse brain neurons. Considering this limitation, we have developed an implantable multimodal sensor that can simultaneously make optical and electrophysiological measurements of the neural activity in the brains of mice. The proposed device integrates a CMOS image sensor and a neural amplifier with a recording electrode into a single chip, making it no more invasive than a conventional implantable CMOS image sensor. The proposed device is based on a 0.35-μm CMOS standard process and occupies an area of 0.50×5.0 mm^2. Furthermore, a hybrid filter is fabricated on the imaging pixel array to remove the excitation light and selectively detect fluorescence. From electrophysiological measurements, we confirm that the neural amplifier features a mid-band gain of 39 dB from 500 mHz to 4 kHz, which is the bandwidth that includes local field and action potentials. Crosstalk noise is observed because of the digital signal used to control the image sensor. However, *in vivo* experiments demonstrate that the device is capable of simultaneously measuring and processing optical and electrophysiological signals when the amplitude spectrum has a peak of less than 1 μV.

1. Introduction

Optical observations of genetically encoded calcium indicator proteins, such as GCaMP, are often used to understand brain functions in mice.(1) Conventional electrophysiological techniques are also used to directly record potential changes that propagate information in the brain.(2) Both methods have merits and limitations. On the one hand, optical observations of GCaMP can record specific cell types, but their temporal resolution is generally poor. On the other hand,

*Corresponding author: e-mail: sasagawa@ms.naist.jp
https://doi.org/10.18494/SAM4264

ISSN 0914-4935
https://myukk.org/

electrophysiological measurements a feature suitable temporal resolution, but it is difficult to focus on specific cell types in extracellular potential measurements. Therefore, multimodal sensor-based optical and electrophysiological recording is required to acquire information that is difficult to measure via a single method and to improve the measurement accuracy.[3,4]

Brain imaging in freely moving mice, i.e., without immobilization, is possible through devices such as miniature microscopes[5] and implantable complementary metal-oxide-semiconductor (CMOS) image sensors (ICISs).[6–8] Although the spatial resolution of ICISs is lower than that of miniature microscopes owing to their lensless construction, their small size and light weight make them considerably less invasive, thus enabling more convenient imaging in freely moving mice. Furthermore, electrophysiological measurement techniques, such as extracellular potential recording, allow brain signals to be monitored through multi-electrode array probes.[9] A simple method for simultaneously recording optical and electrophysiological signals is to implant devices that incorporate both measurement functions.[10,11] However, separate implantation increases invasiveness and makes it difficult to maintain a constant relative position between the devices. Therefore, to prevent increases in sensor dimensions and maintain a constant positional relationship of the observation area, both measurement functions should be integrated into a single sensor.

In this study, we propose the integration of an electrophysiological measurement function into an ICIS to enable simultaneous multimodal measurements without increasing the width of the sensor.

In previous studies, to incorporate electrophysiological measurement functions into an ICIS, Au electrodes were fabricated on the pixel array[12] or next to the image sensor.[13] However, because the electrodes were directly connected to the readout wires in both devices, the distance between the electrode and the neural amplifier was large, introducing crosstalk noise from the image sensor between the electrode and the neural amplifier, which made it difficult to measure extracellular potentials while operating the image sensor.

In the device we designed and fabricated in this study, both an image sensor and neural electrodes are integrated into a single chip, as shown in Fig. 1. The image sensor was designed

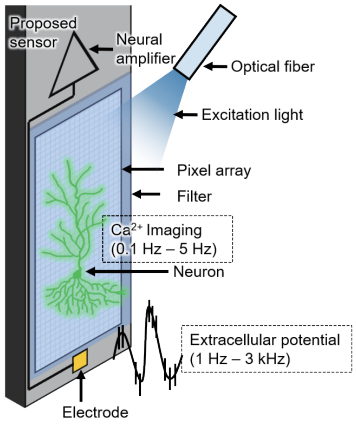

Fig. 1. (Color online) Schematic of the proposed sensor, which integrates an image sensor and a neural amplifier for the simultaneous optical and electrophysiological recording of mouse brain activity. The excitation light is externally delivered through an optical fiber.

using a standard CMOS process, and a neural amplifier was integrated into the same chip. By combining the preamplifiers near the electrodes, a low level of noise can be achieved. The integrated chip is minimally invasive and keeps the relative position of the imaging area and electrodes constant. These features are useful for elucidating the electrophysiological correlations between the changes in the intracellular calcium concentrations of different regions of interest in the mouse brain.

It is difficult to completely suppress the noise radiation because the image sensor is a mixed-signal circuit controlled by a digital signal. However, because the neural amplifier for amplifying weak electrical signals is an analog circuit, it is less affected by the crosstalk noise from the image sensor. In this study, to demonstrate the basic functions of the proposed sensor, we perform simultaneous measurements of fluorescence imaging and extracellular potential through *in vivo* experiments on anesthetized mice.

2. Multimodal Sensing Device

2.1 Chip design

Figure 2 shows a photograph of the proposed multimodal sensor, which was fabricated through a 0.35-μm 2-poly 4-metal CMOS standard process. Table 1 lists the specifications of the sensor.

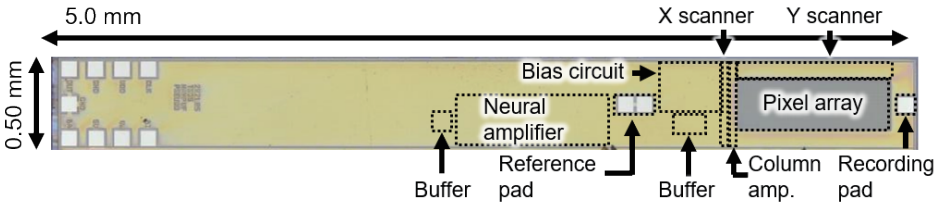

Fig. 2. (Color online) Micrograph of the proposed sensor, which was fabricated using 0.35-μm 2-poly 4-metal CMOS technology. The imaging unit (pixel array, column amp., bias circuit, and buffer) and electrophysiological recording unit (recording pad, reference pad, neural amplifier, and buffer) were integrated into a single chip.

Table 1
Specifications of the fabricated sensor.

CMOS technology	0.35-μm 2-poly 4-metal	
Image sensor	Supply voltage	3.3 V
	Pixel type	3-transistor active pixel sensor
	Photodiode type	N-well/P-substrate
	Pixel size	7.5 × 7.5 μm^2
	Pixel number	40 × 120
Neural amplifier	Supply voltage	5 V
	Gain	39 dB
	Bandwidth	500 mHz–4 kHz

The image sensor circuit is based on an ICIS previously developed in our laboratory. The width, length, and thickness of the sensor are 0.50, 5.0, and 0.13 mm, respectively. Pixels with a size of 7.5 × 7.5 μm^2 were set in a 40 × 120 array, which was deemed sufficiently large for the observation of multiple-neuron activities. The sensor does not include an analog-to-digital converter (ADC) and, hence, outputs voltage as analog signals.

We use an alternating current (AC)-coupled neural amplifier[14] (shown in Fig. 3) to amplify weak electrical signals and eliminate the offset. The closed-loop gain is approximated using the capacitance ratio C_1/C_2. P-channel metal-oxide-semiconductor (PMOS) pseudo-resistors are used as high-value resistors with a small area to bias the operational transconductance amplifier and provide direct current (DC) feedback.

To record the extracellular potential, the recording and reference electrodes are mounted on a pad placed at the top of the chip. A neural amplifier is built into the chip and used as a preamplifier on the active band of extracellular potentials. The analog signals output by the image sensor and neural amplifier are digitized by an external ADC.

2.2 Device fabrication

An emission filter that rejects high-excitation light is required to detect weak fluorescence signals. To reject the excitation light, hybrid, absorption, and interference filters were combined.[15–17] Figure 4 shows the process of fabricating the emission filter on the pixel array. First, a yellow dye (VALIFAST YELLOW 3150; Orient Chemical), solvent (cyclopentanone; Wako), and adhesive (NOA63; Norland Products) were mixed in a weight ratio of 1:2:1. The mixture was subsequently spin-coated on a cover glass at 2000 rpm and cured to form the absorption filter layer with a thickness of ~5 μm. The glass was coated with CYTOP-M as a release layer to easily peel off the filter layer. Next, epoxy resin (Z-1, Nissin) was used to bond the sensor chip onto the absorption filter, which was, in turn, removed from the glass by cutting

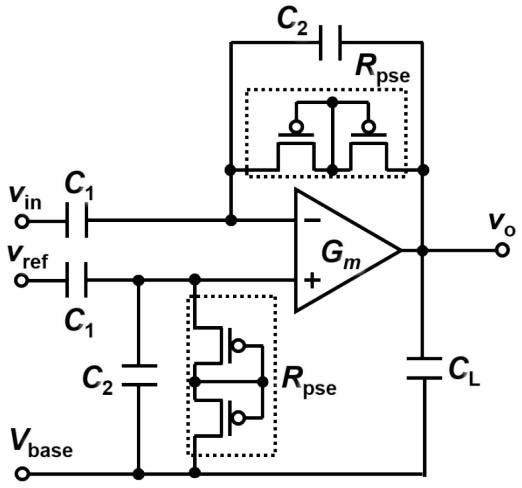

Fig. 3. AC-coupled neural amplifier[14] that rejects DC offset through an input capacitor and amplifies weak extracellular potential signals.

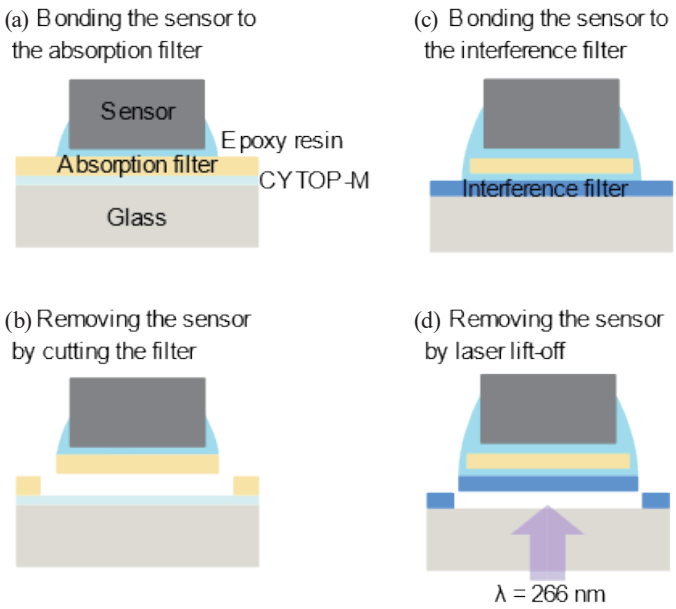

Fig. 4. (Color online) Flowchart of the filter bonding procedure. (a) Bonding sensor and absorption filter to glass. (b) Removing filter from glass. (c) Bonding to interference filter. (d) Removing filter from glass.

the filter. The sensor was subsequently bonded to a long-pass interference filter with a cut-on wavelength of 525 nm using epoxy resin. The interference filter was removed from the fused silica substrate by applying the laser lift-off technique with fourth-harmonic Nd:YAG laser pulses (λ = 266 nm).

For extracellular recording, a Au bump was attached to the pads using a ball bonder (7700D, West bond). Figure 5(a) shows a photograph of the device equipped with the filter and electrode. The recording and reference electrodes were opened to a size of 30 × 30 μm^2 using a Nd: YAG laser (λ = 266 nm), as shown in Fig. 5(b). A black resist was applied around the image sensor to shield it from light.

2.3 Optical imaging function

Figure 6 shows the normalized transmission of the absorption and interference filters obtained using a spectrometer (V-760, JASCO). The results confirm that the filters have a high transmittance for green fluorescence (~520 nm) and cut blue excitation light (~450 nm). Thus, this hybrid filter is highly selective of green fluorescence signals. The excitation light rejection ratio is ~2 × 10^8:1 at 450 nm.

To verify the fluorescence observation function of the proposed device, yellow-green fluorescent beads (F8844, Thermo Fisher) with a diameter of 15 μm were placed on the sensor. The emission peak of these beads was 515 nm, similar to that of neural cells labeled with green fluorescent protein (GFP). The excitation light source was a fiber-output LED (M455F3, THORLABS), and an excitation filter (MF445-45, THORLABS) was used. Figures 7(a) and 7(b) show images of the fluorescent beads observed using a fluorescence microscope and the

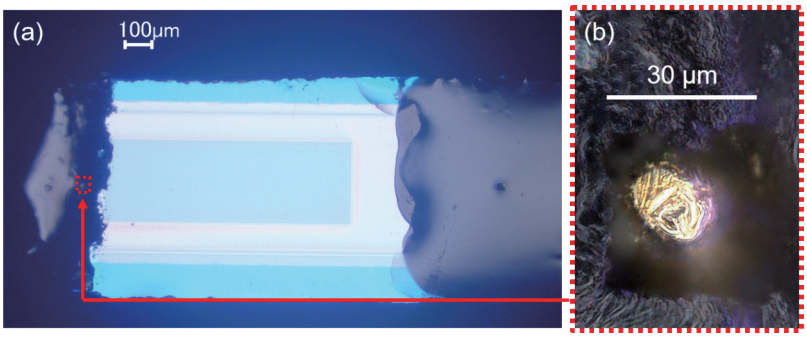

Fig. 5. (Color online) Photographs of the device: (a) attached optical filter and electrode and (b) enlarged view of the electrode. The hybrid filter and electrode are used for fluorescence imaging and extracellular recording. Black resist and epoxy resin were applied to prevent light leakage and a short circuit.

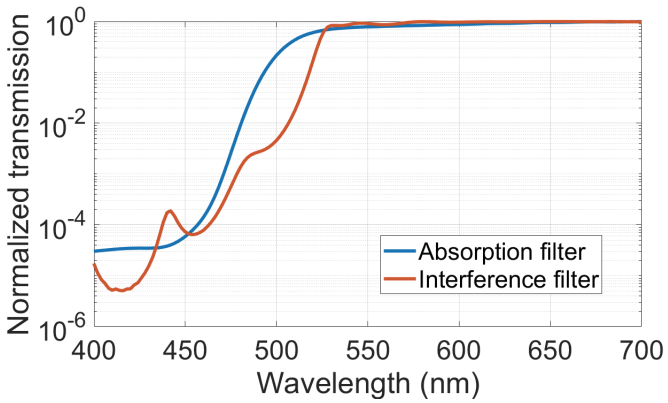

Fig. 6. (Color online) Normalized transmission of the absorption and interference filters in the visible light range. The curves indicate that the filters transmit green fluorescence (~520 nm) and cut blue excitation light (~450 nm).

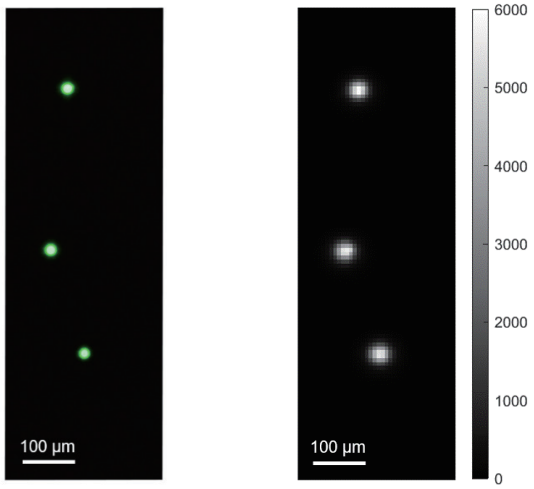

Fig. 7. (Color online) Images of the fluorescent beads captured by (a) fluorescence microscope and (b) proposed sensor. The beads have an emission peak at 515 nm and a diameter of 15 μm. The color bar indicates the pixel values in the proposed sensor. The images demonstrate that the sensor successfully achieved fluorescence imaging.

proposed sensor, respectively. As shown in Fig. 7(b), a clear fluorescent image is obtained using the proposed sensor. The excitation light is rejected by the hybrid filter.

Figure 8(a) shows the image of a single fluorescent bead cropped from Fig. 7(b). Figure 8(b) shows the intensity profile along the red dashed line in Fig. 8(a). The full width at half maximum (FWHM) is ~30 μm, which is larger than the diameter of the fluorescent beads (15 μm). In lensless construction, the spatial resolution deteriorates with increasing distance between the observation target and the sensor. Thus, the observed bead width was larger than the actual bead diameter owing to the filter thickness (~20 μm). This result indicates that, although the resolution of the proposed sensor is insufficient to resolve single neurons in the mouse brain, it is still sufficient to record the activity of multiple-neuron populations distributed over a large imaging area (300 × 900 μm^2).

2.4 Electrophysiological measurement function

Figure 9 shows the impedance–frequency characteristics of the 30 μm^2 bumped aperture of the Au electrode. These characteristics were measured using a potentiostat (PGSTAT204, Metrohm). The thermal noise caused by electrode impedance affects the extracellular potential recording. The impedance at 1 kHz is 300 kΩ, which is sufficiently low for measuring the action and local field potentials (LFPs).[18] Figure 10 shows the gain–frequency response of the neural amplifier. The gain is 39 dB in the band from 500 mHz to 4 kHz. The results show that the measured high-pass cut-off frequency f_L is lower than the simulated value. This is because $f_L = 1/(2\pi R_{pse} C_2)$, which means that the measured pseudo-resistance R_{pse} and capacitance C_2 in the neural amplifier circuit may be higher than the corresponding simulated values. This means that the actual measured values are lower than the simulated ones, indicating that the electrical circuit is less capable of passing low-frequency signals. However, the electrode offset voltage of the DC component can be removed to enable extracellular potential measurements. This gain–frequency characteristic indicates that it is possible to amplify extracellular potentials in frequency bands because LFP and action potential (AP) energy bands are included in the analysis.[19,20]

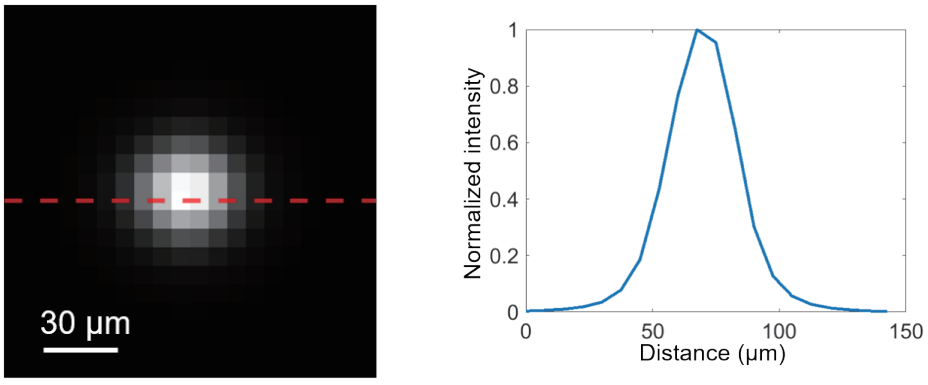

(a) (b)

Fig. 8. (Color online) (a) Image of fluorescent bead and (b) normalized intensity along the bead axis. The intensity curve describes the pixel values along the red dashed line. The diameter of the fluorescence-bead image increases because of the gap from the pixel.

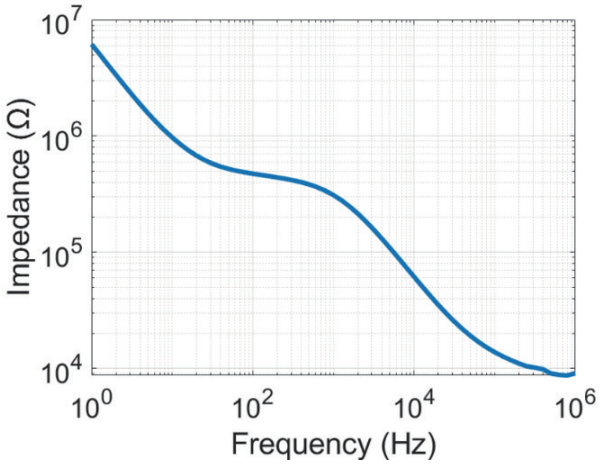

Fig. 9. (Color online) Impedance–frequency characteristics of Au electrode. The impedance at 1 kHz is 300 kΩ, which is sufficiently low for measuring the extracellular potential.

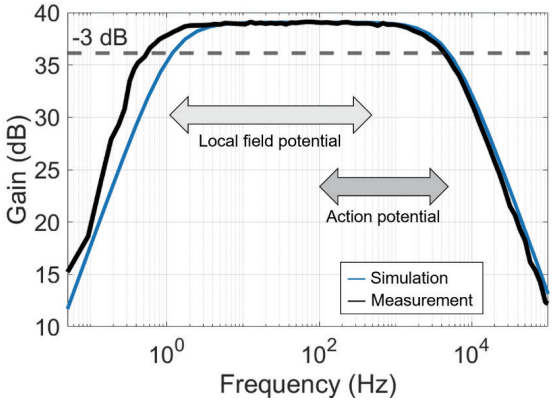

Fig. 10. (Color online) Simulated and measured gain–frequency characteristic curves, including both local field and action potentials. The gain is approximately 39 dB for the band between 500 mHz and 4 kHz.

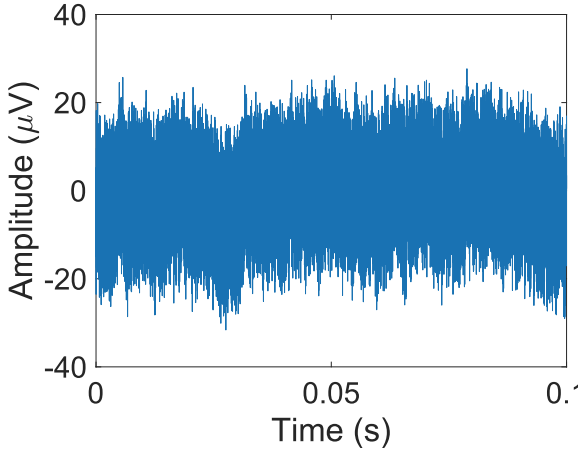

Fig. 11. (Color online) Input-referred noise voltage of the neural amplifier. The amplitude corresponds to the output noise divided by the amplifier gain. The RMS value is approximately 5 μVrms.

Figure 11 shows the input-referred noise voltage of the neural amplifier. The root-mean-square (RMS) value is ~5 μVrms, which is sufficiently low compared with the typical extracellular background noise of 10 μVrms. Therefore, through these experiments, we have determined that the proposed sensor can effectively amplify the extracellular potential for electrophysiological recording.

3. Demonstration of *In Vivo* Measurement

All animal experiments (n = 4) were performed in accordance with the protocols approved by Nara Institute of Science and Technology (NAIST). GCaMP6 mice [strain: FVB-Tg(Thy1-GCaMP6)5Shi., provided by RIKEN BRC through the National Bio-Resource Project of MEXT, Japan[21]] were anesthetized with urethane before device implantation and during brain activity measurements. The mice were all male and aged 13 to 17 weeks. The device was implanted above the hippocampus (anteroposterior: −2.0 mm, mediolateral: 1.8 mm) using a microdrill and a micromanipulator (DMA-1551, Narishige). The sensor was positioned on the basis of the mouse brain atlas and inserted so that the recording electrode rested at a depth of approximately 2 mm from the surface of the brain. Kainic acid (10 mg/kg) was administered intraperitoneally for stimulation. The sensors were implanted in all the animal subjects following the same procedure

Figure 12 shows a cross-sectional diagram of the sensor implantation and a block diagram of the simultaneous measurement system. Imaging and extracellular recording were simultaneously performed in the CA1 and CA3 regions, respectively. An optical fiber was inserted at an angle of 30–40° from the sensor (anteroposterior: −2.0 mm, mediolateral: 1.8 mm) to deliver excitation light. The excitation light source was a fiber-output LED (M455F3, THORLABS) with an excitation filter (MF445-45, THORLABS), which was controlled by an LED driver (LEDD1B, THORLABS) with a constant current (~600 mA). The output of the sensor was buffered outside the chip. The image and extracellular potential were recorded at 10 fps and 20 ksps, respectively. The chip input and output pads were connected to the external buffer board via Al wires. The buffer board comprises operational amplifiers and regulators soldered to a universal board. Since the experiments were conducted under anesthesia, the effects of the size and weight of this

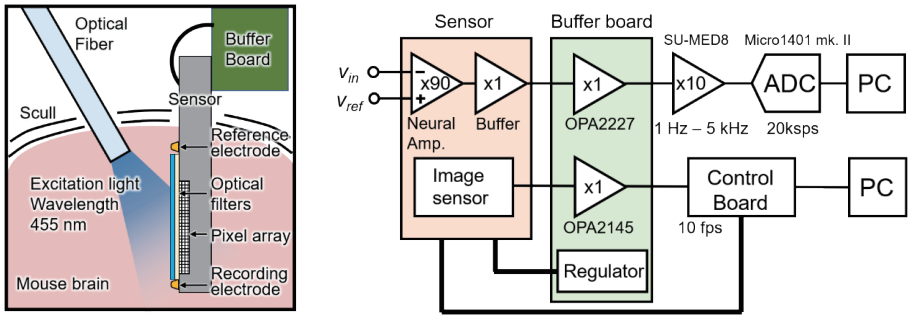

(a) (b)

Fig. 12. (Color online) Animal experimental setup. (a) Cross-sectional view of the implanted sensor. (b) Simultaneous recording system. The sensor was implanted directly into the mouse's brain. An optical fiber was implanted as excitation light. The sensor analog output was digitalized by an external ADC after buffering.

external buffer were not taken into account. To avoid short circuits, the sensor was covered with epoxy resin (Z-1, Nissin) except for the imaging and pad areas. Epoxy resin was also used as an adhesive.

While driving both the neural amplifier and the image sensor simultaneously, crosstalk noise from the image sensor is amplified by the neural amplifier and appears in the output. Figure 13 shows the spectra of the extracellular potentials measured in the mouse brain before the recording electrode reached CA3. The results obtained when the image sensor was in the ON and OFF states were compared. Each spectrum is the average of 10 measurements lasting 1 s each. When the image sensor was turned on, a slight increase (<1 μV) was observed in the amplitude spectrum above 1 kHz. Because the clock signal of the image sensor is repeated, the crosstalk noise is assumed to be a pattern noise. Pattern noises, including crosstalk noise, can be reduced by spectral subtraction.[20] However, this result indicates that simultaneous recording is possible because the extracellular potential can be measured with almost no effect of the crosstalk noise caused by the image sensor.

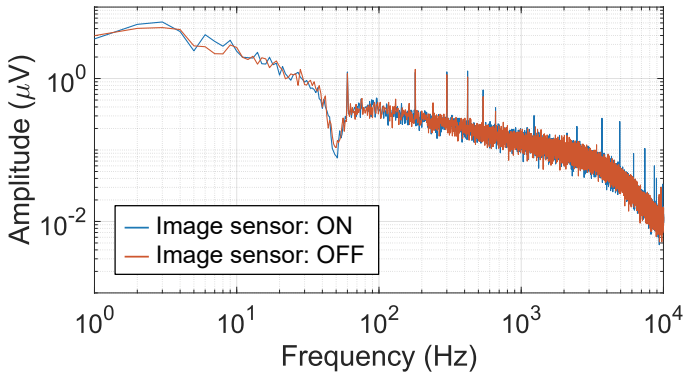

Fig. 13. (Color online) Comparison of spectra of extracellular potentials to determine the effect of crosstalk noise caused by the image sensor. A slight increase in amplitude was observed when turning on the image sensor.

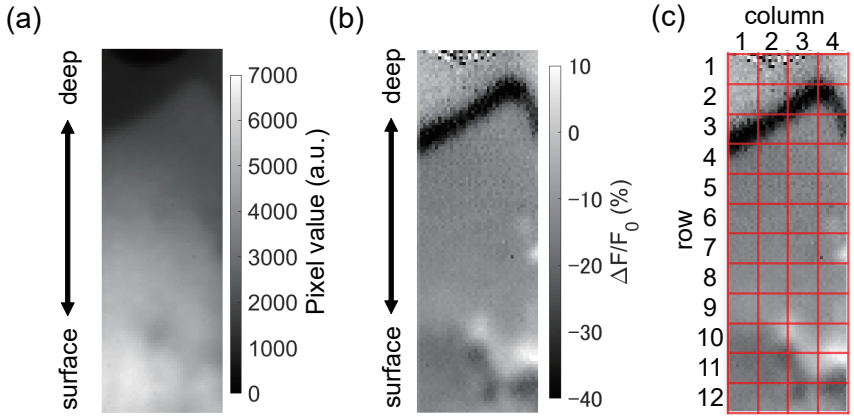

Fig. 14. (Color online) Fluorescence images of the brain: (a) reference F_0 condition, (b) $\Delta F/F_0$ observed 30 min after stimulation, and (c) sectioned imaging area used for analysis. The proposed sensor can capture optical patterns in the imaging area owing to its 40 × 120 pixels.

Figure 14(a) shows the average image of 10 frames immediately before stimulation. Figure 14(b) shows the fluorescence ratio image ($\Delta F/F_0$) around the CA1 region after 30 min of stimulation. The upper side of this image is the deep brain side, and the lower side is the superficial side. The fluorescence difference (ΔF) is defined as the difference between $F(t)$ and F_0, where F is the pixel value and F_0 is the average of the pixel values in the 10 frames immediately before the stimulation. The image shown in Fig. 14(b) contains bright and dark regions, showing that, owing to the multiple pixels, it is possible to observe groups of neurons distributed in different areas of the image sensor surface. To analyze the changes in fluorescence intensity at different locations, the imaging area is divided into 12 × 4 sections, each containing 10 × 10 pixels, as shown in Fig. 14(c).

Figure 15 shows the fluorescence ratios $\Delta F/F_0$ in the different sections indicated in Fig. 14(c). The random noise was reduced by averaging the values of the 100 pixels in each cell. In addition, a moving average of five frames was obtained. In sections (row, col) = (3, 1), (3, 2), (2, 3), and (2, 4), $\Delta F/F_0$ decreased. However, in (row, col) = (10, 3), (11, 4), $\Delta F/F_0$ increased. This result suggests that the imaging device can detect the difference in fluorescence in each region.

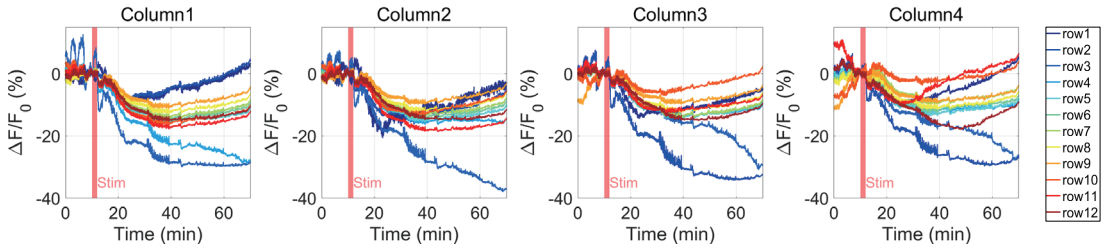

Fig. 15. (Color online) Fluorescence ratios in different sections of the imaging area for a stimulation time of 10 min. The 4 × 12 ROIs exhibited different changes in fluorescence ratio.

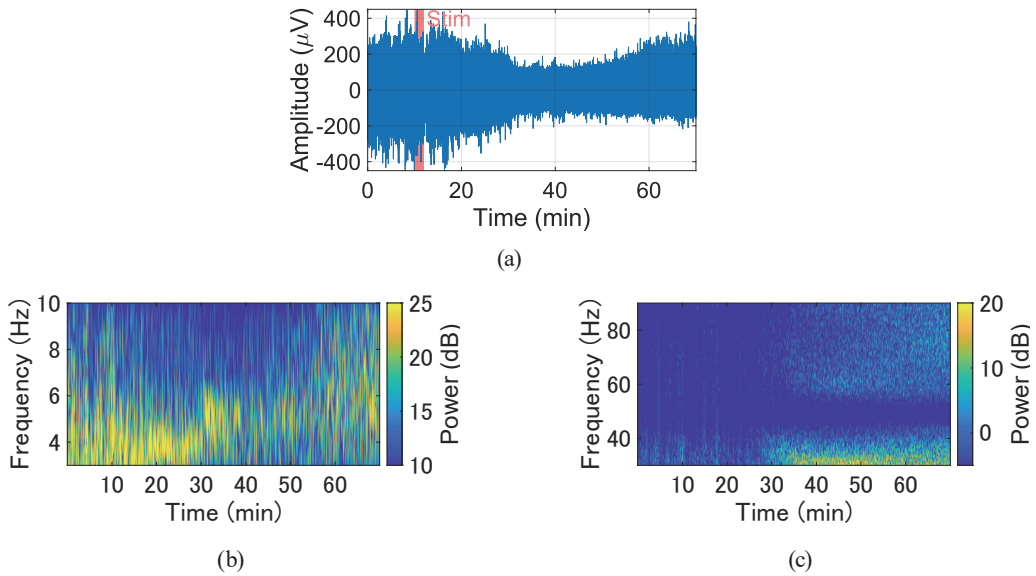

Fig. 16. (Color online) (a) Extracellular raw data recording. (b) Theta (c) and gamma band spectrograms. The stimulation time was adjusted to 10 min. After stimulation, the amplitude gradually changed. The power of the theta and gamma wave bands (3–10 and 30–90 Hz, respectively) also changed.

Figure 16(a) shows the waveform of the extracellular potential recording. After stimulation for t = 10 min, the amplitude gradually decreased from t = 10 and t = 30 min. Similar results were obtained for multiple trials (n = 4). The amplitude recovered at t ~ 60 min as shown in the figure.

Figures 16(b) and 16(c) are spectrograms of the band-passed data in the theta wave band (3–10 Hz) and gamma wave band (30–90 Hz), respectively. Pattern noise was reduced by spectral subtraction. The theta wave weakened at t = 40 min and subsequently increased slightly. Moreover, the gamma wave intensity increased after t = 30 min. The low power of the gamma band at ~50 Hz is attributed to the notch filter of SU-MED8 used as an amplifier before ADC.

These electrophysiological recordings demonstrate that the proposed sensor can detect extracellular potential changes with no significant effect of the crosstalk noise from the clock signal of the image sensor.

4. Discussion

Figures 14 and 15 show optical recordings, whereas Fig. 16 shows electrophysiological recordings. Figure 14 shows images of the reference fluorescence F_0 and fluorescence ratio $\Delta F/F_0$ after 30 min of stimulation. These results demonstrate that the sensor can detect the spatial contribution of the light intensity across the imaging area. Figure 15 shows the temporal change in $\Delta F/F_0$ in different ROIs. Figure 16 shows the temporal changes in the amplitude and frequency of the electrical signals recorded by the electrode located 100 μm from the edge of the pixel array. As shown in Figs. 15 and 16, the proposed sensor effectively achieves the simultaneous measurement of changes in fluorescence intensity and extracellular potential. As shown in Fig. 13, the peak of the amplitude spectrum of the crosstalk noise is low (less than 1 μV), and the effect of digital noise from the image sensor can be reduced by removing the pattern noise, including the crosstalk noise, through spectral subtraction.

Because of the kainic acid injection, the shifted image in Fig. 14 is attributed to brain edema,[22] and the increase in amplitude from t = 30 to 40 min in Fig. 15 appeared to be due to slow flashes.[23] The changes in extracellular potential shown in Fig. 16 have also been observed in previous studies.[24–26]

The sensor enables the simultaneous measurement of optical and electrophysiological signals while avoiding an increase in sensor width. The proposed sensor is expected to expand the range of experimental performance and contribute to the development of neuroscience.

Although the simultaneous measurement of imaging and extracellular potential has been demonstrated, the Au recording electrode is ~100 μm from the edge of the pixel array. Therefore, the correlation between extracellular potential measurements and imaging results is not particularly high. However, an LFP signal can be observed from a wide range; thus, we would like to conduct more experiments on animals to show a statistically significant difference between fluorescent ratios and the extracellular potential change to investigate various correlations. Additionally, to solve the problem of distance, the top metal layer that constitutes the pixel array can be laid out as a signal line for measuring the extracellular potential.[12]

In addition, because of contact imaging, the spatial resolution of the sensor deteriorates as its distance from the object under observation increases. To solve this problem, an angle-selective pixel array can be used to suppress the degradation of spatial resolution while maintaining a constant sensor size.[27]

In this paper, for simple construction, we used an optical fiber as an external light source; however, integrating the light source is also an important factor in reducing invasiveness. The utilization of μLEDs is one of the useful methods for integrating a light source.[28] However, μLEDs have a wide emission wavelength range. Therefore, a configuration that combines a μLED with an excitation filter could help solve the problem.[29]

5. Conclusions

In this study, we have developed an implantable multimodal sensor that simultaneously records fluorescence images and extracellular potentials of the mouse brain. The sensor is fabricated using a 0.35-μm CMOS standard process and features an elongated shape that is suitable for implantation in a mouse brain. The basic imaging and electrophysiological recording functions are successfully achieved. We also confirmed that a neural amplifier integrated into the ICIS has suitable specifications for performing extracellular recordings. *In vivo* experiments were conducted to verify the capacity of the proposed sensor to simultaneously record optical and electrophysiological readings. The effect of crosstalk noise was minimal, and the proposed sensor achieved the simultaneous measurement of fluorescent ratios and extracellular potential.

The reduced size of the sensor makes it possible to conduct experiments on freely moving mice without burdening them, which is useful for understanding the correlations between mouse behaviors and calcium imaging or electrophysiological recordings of the brain region of interest.

Acknowledgments

This work was supported by JSPS KAKENHI (Grant Numbers JP18H03780, JP20J23439, and JP21H03809), JST-CREST (JPMJCR1654), the VLSI Design and Education Center (VDEC), and the University of Tokyo, in collaboration with the Cadence Corporation and Mentor Graphics Corporation.

References

1 H. Dana, T.-W. Chen, A. Hu, B. C. Shields, C. Guo, L. L. Looger, D. S. Kim, and K. Svoboda: PLoS One **9** (2014) e108697. https://dx.plos.org/10.1371/journal.pone.0108697
2 G. Buzsáki, C. A. Anastassiou, and C. Koch: Nat. Rev. Neurosci. **13** (2012) 407. http://www.nature.com/articles/nrn3241
3 Z. Ramezani, K. J. Seo, and H. Fang: J. Micromech. Microeng. **31** (2021) 044002. https://iopscience.iop.org/article/10.1088/1361-6439/abeb30
4 M. J. Donahue, A. Kaszas, G. F. Turi, B. Rózsa, A. Slézia, I. Vanzetta, G. Katona, C. Bernard, G. G. Malliaras, and A. Williamson: eNeuro **5** (2018) ENEURO.0187. http://eneuro.org/lookup/doi/10.1523/ENEURO.0187-18.2018
5 K. K. Ghosh, L. D. Burns, E. D. Cocker, A. Nimmerjahn, Y. Ziv, A. El Gamal, and M. J. Schnitzer: Nat. Methods **8** (2011) 871. http://www.nature.com/articles/nmeth.1694

6 J. Ohta, Y. Ohta, H. Takehara, T. Noda, K. Sasagawa, T. Tokuda, M. Haruta, T. Kobayashi, Y. M. Akay, and M. Akay: Proc. IEEE **105** (2017) 158. http://ieeexplore.ieee.org/document/7524734/
7 R. Rebusi, J. P. Olorocisimo, J. Briones, Y. Ohta, M. Haruta, H. Takehara, H. Tashiro, K. Sasagawa, and J. Ohta: Front. Neurosci. **15** (2021) Article 667708. https://www.frontiersin.org/articles/10.3389/fnins.2021.667708/full
8 M. C. Guinto, M. Haruta, Y. Kurauchi, T. Saigo, K. Kurasawa, S. Ryu, Y. Ohta, M. Kawahara, H. Takehara, H. Tashiro, K. Sasagawa, H. Katsuki, and J. Ohta: J. Biomed. Opt. **27** (2022) 026501. https://www.spiedigitallibrary.org/journals/journal-of-biomedical-optics/volume-27/issue-02/026501/Modular-head-mounted-cortical-imaging-device-for-chronic-monitoring-of/10.1117/1.JBO.27.2.026501.full
9 K. D. Wise, A. M. Sodagar, Ying Yao, M. N. Gulari, G. E. Perlin, and K. Najafi: Proc. IEEE **96** (2008) 1184. http://ieeexplore.ieee.org/document/4545308/
10 L. F. Cobar, A. Kashef, K. Bose, and A. Tashiro: Sci. Rep. **12** (2022) 736. https://doi.org/10.1038/s41598-021-04365-7
11 A. A. Patel, N. McAlinden, K. Mathieson, and S. Sakata: Front. Neurosci. **14** (2020) 148. https://www.frontiersin.org/article/10.3389/fnins.2020.00148/full
12 A. Tagawa, M. Mitani, H. Minami, T. Noda, K. Sasagawa, T. Tokuda, and J. Ohta: Jpn. J. Appl. Phys. **49** (2010) 04DL02. https://iopscience.iop.org/article/10.1143/JJAP.49.04DL02
13 K. Naganuma, Y. Ohta, T. E. Murakami, R. Okada, M. C. Guinto, H. Takehara, M. Haruta, H. Tashiro, K. Sasagawa, Y. Sunaga, Y. M. Akay, M. Akay, and J. Ohta: Sens. Mater. **34** (2022) 1561. https://sensors.myu-group.co.jp/article.php?ss=3710
14 R. R. Harrison and C. Charles: IEEE J. Solid-State Circuits **38** (2003) 958. http://ieeexplore.ieee.org/document/1201998/
15 K. Sasagawa, A. Kimura, M. Haruta, T. Noda, T. Tokuda, and J. Ohta: Biomed. Opt. Express **9** (2018) 4329. https://opg.optica.org/abstract.cfm?URI=boe-9-9-4329
16 K. Sasagawa, E. Rustami, Y. Ohta, M. Haruta, H. Takehara, H. Tashiro, and J. Ohta: Electron. Commun. Jpn. **104** (2021) e12313. https://onlinelibrary.wiley.com/doi/10.1002/ecj.12313
17 E. Rustami, K. Sasagawa, K. Sugie, Y. Ohta, M. Haruta, T. Noda, T. Tokuda, and J. Ohta: IEEE Trans. Circuits Syst. I Regul. Pap. **67** (2020) 1082. https://ieeexplore.ieee.org/document/9016253/
18 J. P. Neto, P. Baião, G. Lopes, J. Frazão, J. Nogueira, E. Fortunato, P. Barquinha, and A. R. Kampff: Front. Neurosci. **12** (2018) 715. https://www.frontiersin.org/article/10.3389/fnins.2018.00715/full
19 G. Orbán, D. Meszéna, K. R. Tasnády, B. Rózsa, I. Ulbert, and G. Márton: PLoS One **14** (2019) e0221510. https://dx.plos.org/10.1371/journal.pone.0221510
20 T. Wichmann: J. Neurosci. Methods **98** (2000) 57. https://linkinghub.elsevier.com/retrieve/pii/S0165027000001904
21 M. Ohkura, T. Sasaki, J. Sadakari, K. Gengyo-Ando, Y. Kagawa-Nagamura, C. Kobayashi, Y. Ikegaya, and J. Nakai: PLoS One **7** (2012) e51286. https://dx.plos.org/10.1371/journal.pone.0051286
22 F. Seitelberger, H. Lassmann, and O. Hornykiewicz: Acta Neurobiol. Exp. (Wars) **50** (1990) 263. http://www.ncbi.nlm.nih.gov/pubmed/2130648
23 X. Zhang, Z. Qiao, N. Liu, L. Gao, L. Wei, A. Liu, Z. Ma, F. Wang, S. Hou, J. Li, and H. Shen: Sci. Rep. **9** (2019) 4518. http://www.nature.com/articles/s41598-019-41241-x
24 L. Li, K. Kriukova, J. Engel, and A. Bragin: Sci. Rep. **8** (2018) 1423. http://dx.doi.org/10.1038/s41598-018-19675-6
25 T. K. Berdyyeva, E. P. Frady, J. J. Nassi, L. Aluisio, Y. Cherkas, S. Otte, R. M. Wyatt, C. Dugovic, K. K. Ghosh, M. J. Schnitzer, T. Lovenberg, and P. Bonaventure: Front. Neurosci. **10** (2016) 53. http://journal.frontiersin.org/Article/10.3389/fnins.2016.00053/abstract
26 J. Eller, S. Zarnadze, P. Bäuerle, T. Dugladze, and T. Gloveli: PLoS One **10** (2015) e0123636. https://dx.plos.org/10.1371/journal.pone.0123636
27 K. Sugie, K. Sasagawa, M. C. Guinto, M. Haruta, T. Tokuda, and J. Ohta: Electron. Lett. **55** (2019) 729. https://onlinelibrary.wiley.com/doi/10.1049/el.2019.1031
28 F. Wu, E. Stark, P.-C. Ku, K. D. Wise, G. Buzsáki, and E. Yoon: Neuron **88** (2015) 1136. https://linkinghub.elsevier.com/retrieve/pii/S0896627315009265
29 M. I. Azmer, K. Sasagawa, E. Rustami, K. Sugie, Y. Ohta, M. Haruta, H. Takehara, H. Tashiro, and J. Ohta: Jpn. J. Appl. Phys. **60** (2021) SBBG07. https://iopscience.iop.org/article/10.35848/1347-4065/abe5bf

About the Authors

Kenji Sugie received his B.S. degree in electrical and electronic engineering from Ritsumeikan University, Shiga, Japan, and his M.E. degree from Nara Institute of Science and Technology (NAIST), Nara, Japan. He is currently pursuing his Ph.D. degree at NAIST at the Photonic Device Science Laboratory. His research interests include implantable devices for neural activity observation. (sugie.kenji.sb5@ms.naist.jp)

Kiyotaka Sasagawa received his B.S. degree from Kyoto University in 1999 and his M.E. and Ph.D. degrees in materials science from NAIST, Japan, in 2001 and 2004, respectively. He then became a researcher with the National Institute of Information and Communications Technology, Tokyo. In 2008, he joined NAIST as an assistant professor, where he has been an associate professor since 2019. His research interests involve bioimaging, biosensing, and electromagnetic field imaging. (sasagawa@ms.naist.jp)

Ryoma Okada received his B.E. degree in electrical and electronic engineering from Shizuoka University, Shizuoka, Japan, and his M.E. degree from Nara Institute of Science and Technology (NAIST), Nara, Japan. He is currently pursuing his Ph.D. degree at the Photonic Device Science Laboratory in NAIST. His current research interests involve polarization image sensors and electromagnetic field imaging. (okada.ryoma.on9@ms.naist.jp)

Yasumi Ohta received her B.S. degree in physics from Nara Women's University in 1984. She enrolled in the Faculty of Science at Kyoto University in 2004 and switched to the master's program at the Graduate School of Science, Kyoto University in 2006. She received her M.S. and Ph.D. degrees in biophysics from Kyoto University, Kyoto, Japan, in 2008 and 2011, respectively. From 1984 to 1986, she worked at Mitsubishi Electric Corp., Hyogo, Japan. In 2011, she joined Nara Institute of Science and Technology (NAIST), Nara, Japan, as a postdoctoral fellow. Her research interests include implantable bioimaging CMOS sensors and neuroscience. (ohtay@ms.naist.jp)

Hironari Takehara received his B.E. and M.E. degrees in applied chemistry from Kansai University, Osaka, Japan, in 1984 and 1986, and his Ph.D. degree in materials science from Nara Institute of Science and Technology (NAIST), Nara, Japan in 2015, respectively. From 1986 to 2012, he was a semiconductor process engineer at Panasonic Corporation, Kyoto, Japan, where he developed BiCMOS, high-voltage SOI, and optoelectronic IC processes. In 2015, he joined NAIST as a postdoctoral fellow and he has been an assistant professor since 2019. His current research interests involve CMOS image sensors and bioimaging. (t-hironari@ms.naist.jp)

Makito Haruta received his B.E. degree in bioscience and biotechnology from Okayama University, Okayama, Japan, in 2009, and his M.S. degree in biological science and Dr. Eng. degree in material science from Nara Institute of Science and Technology (NAIST), Nara, Japan, in 2011 and 2014, respectively. He was a postdoctoral fellow with NAIST from 2014 to 2016. He joined the Institute for Research Initiatives, NAIST, in 2016, as an assistant professor. In 2019, he joined the Graduate School of Science and Technology, NAIST, as an assistant professor. His research interests include brain imaging devices for understanding brain functions related to animal behaviors. (m-haruta@ms.naist.jp)

Hiroyuki Tashiro received his B.E. and M.E. degrees in electrical and electronic engineering from Toyohashi University of Technology (TUT), Aichi, Japan, in 1994 and 1996, respectively. He received his Ph.D. degree in engineering from Nara Institute of Science and Technology (NAIST), Nara, Japan, in 2017. In 1998, he joined Nidek Co., Ltd., Aichi, Japan, where he worked on the research and development of ophthalmic surgical systems and retinal prostheses. In 2004, he became an assistant professor at the Faculty of Medical Sciences, Kyushu University, Fukuoka, Japan, and since 2019, he has been an associate professor at NAIST. His current research interests include artificial vision systems and neural interfaces.
(tashiro.hiroyuki.289@m.kyushu-u.ac.jp)

Jun Ohta received his B.E., M.E., and Dr. Eng. degrees in applied physics from The University of Tokyo, Japan, in 1981, 1983, and 1992, respectively. In 1983, he joined Mitsubishi Electric Corporation, Hyogo, Japan. From 1992 to 1993, he was a visiting scientist with the Optoelectronics Computing Systems Center, University of Colorado Boulder. In 1998, he joined the Graduate School of Materials Science, Nara Institute of Science and Technology (NAIST), Nara, Japan, as an associate professor, where he was appointed as a professor in 2004. His current research interests include smart CMOS image sensors for biomedical applications and retinal prosthetic devices. He is a Fellow of IEEE, the Japan Society of Applied Physics, and the Institute of Image, Information, and Television Engineers. (ohta@ms.naist.jp)